Comprehensive EUV Lithography Model

Mark D. Smith, Trey Graves, John Biafore, Stewart Robertson
KLA-Tencor Corp.

Cheolkyun Kim, James Moon, Jaeheon Kim, Cheolkyu Bok, Donggyu Yim
Hynix Semiconductor Corp.

ABSTRACT

As EUV lithography nears pilot-line stage, photolithography modeling becomes increasingly important in order for engineers to build viable, production-worthy processes. In this paper, we present a comprehensive, calibrated lithography model that includes optical effects such as mask shadowing and flare, combined with a stochastic resist model that can predict effects such as line-edge roughness. The model was calibrated to CD versus pitch data with varying levels of flare, as well as dense lines with varying degrees of mask shadowing. We then use this model to investigate several issues critical to EUV. First, we investigate EUV photoresist technology: the impact of photoelectron-PAG exposure kinetics on photospeed, and then we examine the trade-off between LWR and photospeed by changing quencher loading in the photoresist model. Second, we compare the predicted process windows for dense lines as flare and lens aberrations are reduced from the levels in the current alpha tools to the levels expected in the beta tools. The observed interactions between optical improvements and resist LWR indicate that a comprehensive model is required to provide a realistic evaluation of a lithography process.

Introduction

Historically, the semiconductor industry has maintained Moore's law by using a either an increase in numerical aperture (NA) or a reduction in wavelength (λ). The next planned technology change is from ArF to EUV. The dramatic reduction in wavelength combined with a reduction in NA has obvious advantages for resolution and depth of focus, but it also leads to optical and physical effects that were practically insignificant in ArF tools. For example, lens aberrations are inversely proportional to the wavelength – a 1.5nm RMS wavefront error at 193nm wavelength corresponds to around 8 milliwaves of aberration, while the same error at 13.5nm wavelength is more than 100 milliwaves. The scaling for flare is much worse – flare levels are inversely proportional to the wavelength squared. Furthermore, EUV scanners use a reflective mask, which leads to a shadowing effect that depends on feature orientation and field position. These optical effects were either absent or a minor effect on ArF toolsets. For memory manufacturing, this means that we cannot apply the same OPC corrections to every cell. Instead, these effects must be characterized and modeled, so that different corrections can be applied across the field.

There are also new manufacturing challenges for EUV, including throughput, CD uniformity (CDU), and line-width roughness (LWR). These problems are all closely tied to the power that can be supplied by the EUV source, because lower power means either a lower scan rate (which is detrimental to throughput) or a lower exposure dose (which leads to poor CDU and LWR due to photon shot noise). Photoresist vendors are working directly on this problem, as they try to determine the right compromise between resolution, LWR, and sensitivity.

With all of these new optical and physical effects, photolithography simulation can be an invaluable tool for the photolithography engineer. Under normal circumstances, much of the learning required to build a viable process can be obtained by a large, extensive set of experiments. For EUV, it is not possible to use experiments alone because there are so many new effects, and experimental data is currently very hard to obtain. Simulation can be used to optimize a virtual

Extreme Ultraviolet (EUV) Lithography II, edited by Bruno M. La Fontaine, Patrick P. Naulleau, Proc. of SPIE
Vol. 7969, 796906 · © 2011 SPIE · CCC code: 0277-786X/11/$18 · doi: 10.1117/12.879766

process. This set of virtual operating conditions is not expected to be a manufacturable process, but rather a starting point that will allow us to determine the most important trade-offs and to reduce the number of experiments required to optimize a real process.

In this paper we give an example of a comprehensive EUV lithography model that includes all of the effects described in this introduction. In the next section, we describe the experimental dataset used to generate the model, and we show a comparison of the model to both CD and LWR experimental data. Next, we investigate two different changes to the process. First, we investigate improvements in photoresist technology by perturbing the parameters in the calibrated resist model. We modify the exposure kinetics to see the interaction between increased acid yield and "photoelectron blur", and then we vary the formulation in the photoresist model by changing quencher loading. Second, we investigate the impact of reducing lens aberrations and flare process windows and LWR. Finally, we present a summary and offer our conclusions.

Experimental Dataset and Model Calibration

Wafers were exposed on the EUV ADT at IMEC during 2008. The exposure settings on this tool are NA=0.25 and 0.5 partial coherence. The experimental film stack was 65nm of photoresist on bare silicon. A special EUV flare reticle was designed and manufactured by Hynix, and the structures on this mask are shown in Figure 1. In this study, we focused on the flare test structure and the mask shadowing test structure. Within the flare test structure, there are 100 x 100 micron regions with varying degrees of fill from 100% open (all reflector) to 0% open (all absorber) surrounding a 10 x 10 micron region with line-space test structures. We collected CD data for vertical patterns from the middle of the field. This corresponds to patterns with no shadowing at the mask (the chief ray is aligned with the direction of the lines). Within the shadowing test structure, we collected CD data for vertical, horizontal, and diagonal dense lines for 28nm, 32nm, and 40nm half-pitch (HP). Data was collected from all seven test layouts across the full width of the field, which results in varying degrees of mask shadowing. The LWR was also measured for the vertical features in the center of the field for the shadowing test structure.

Mask measurements were not available for all of the test structures in this experiment. Some measurements were available for similar structures, and a mask bias of around 2 to 3nm (wafer scale) was typical. For the smallest structures (27nm lines), a bias of -1nm was observed. For this study, we used a constant 3nm bias on all features, except for the 28nm shadow structure, where a 1nm bias was applied.

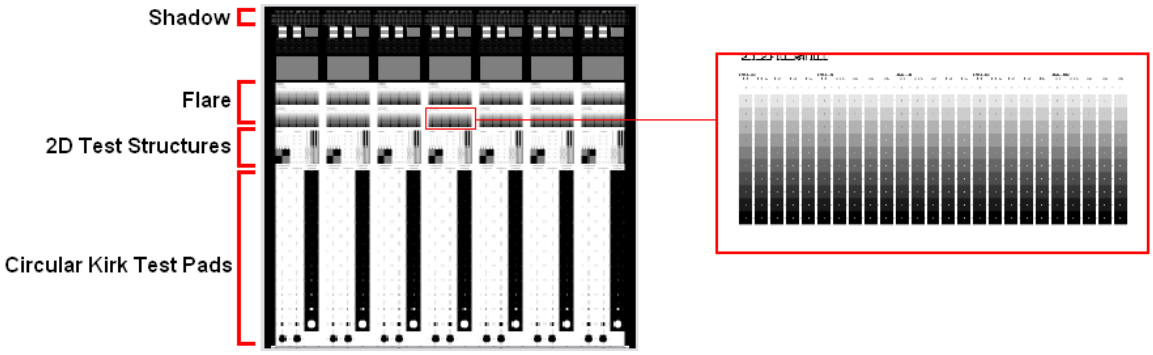

Figure 1: The EUV test reticle is composed of seven identical, vertical layouts. Within each layout is a shadowing test structure, a flare test structure, a set of 2D test patterns (such as line-end shortening), and a flare Kirk test pattern. The pattern density for the full field is shown on the left, and on the right is a detail of the flare pattern density test structure.

PROLITH X3.2 was used to model this set of experimental data. To describe the long-range flare found in EUV exposure tools, we used a flare point spread function approach. This flare model can be derived from statistical optics [1,2,3], and has been used elsewhere to describe ArF and EUV exposure systems [2,3,4,5]. The flare at a particular point in the field is calculated as a convolution of a flare point spread function (PSF) with the image at the wafer without flare:

$$Flare = I_{ideal}(x, y) \otimes PSF(r) \tag{1}$$

We fit a fractal-shaped flare PSF to Kirk test data [3,5]:

$$PSF(r) = \frac{K}{r^{n+1}} \quad for \; r > r_{\min} \tag{2}$$

$$K = \frac{(n-1)TIS\, r_{\min}^{n-1}}{2\pi}$$

The total integrated scatter (*TIS*) was found to be 16.9% with a spectral index (n) of 1.15, which are typical of other published data for this toolset [6,7,8]. The parameter r_{min} is the boundary between low-frequency phase errors which are modeled by lens aberrations and high-frequency phase errors modeled as flare. We selected r_{min}=0.2 microns. Because the PSF for EUV exposures has a very long range (perhaps the entire field or even into adjacent fields), calculation of the image at the wafer over such a large range is intractable. Instead, we calculate a rigorous image to a specified cutoff distance outside of our region of interest, and then outside of this cutoff we approximate the image at the wafer by calculating the pattern density from the layout. We used the software AreaFill [9] to construct these pattern densities from the OASIS layout file. Typically, two pattern density maps were used – a long range map with a large pixel size of 100 microns for the full field, and a medium range map with a small pixel size of 5 microns. This approach has been used elsewhere and demonstrated to be very accurate [8,10]. The two pattern density maps for simulation of the flare test structures are shown in Figure 1. The coarse, full-field pattern density in Figure 1 was also used for the shadow test structures, but with a different medium range pattern density map. The flare PSF combined with these pattern densities was used to evaluate equation (1) and simulate the long-range and medium-range flare in all of the results shown in this study. To describe the topography on the mask, we used an approximate, thick mask topography algorithm similar to the method described by Adam and Neureuther [11]. This model is both fast and accurate, and can be applied to both 1D and 2D test structures. Finally, we used the PROLITH Stochastic Resist Model (SRM) to describe the photoresist and resist processing steps [13,14,15].

The model was calibrated using AutoTune™ from KLA-Tencor Corp. The starting parameters in the Stochastic Resist Model were chosen to be typical values, and then converged using nonlinear least-squares regression. The first simulations with the model showed large deviations with experimental data for the larger features, such as 60nm and 80nm lines through pitch. Large deviations were also observed for the line-end shortening structures. A large amount of the error between the simulated and experimentally observed CD values could be corrected by introducing lens aberrations and defocus. This dataset only contained a single focus and dose, so the defocus in the model may represent an actual defocus present during the experiment. In addition, this tool has been reported to have around 1.4nm RMS wavefront aberration [16]. This corresponds to 107 milliwaves, which is not insignificant. Thus, we felt that calibration of simple aberrations, such as spherical and astigmatism, as well as calibration of defocus was justified. Of course, a more accurate approach would be to run a full focus-exposure experiment and to also use measured lens aberrations, but neither of these were available. The results are shown in Figures 2 to 4. Now that we have a reasonable model for the scanner and photoresist, we use the model to predict what kind of improvements we might see in the lithography when advances in photoresist and scanner technology are realized.

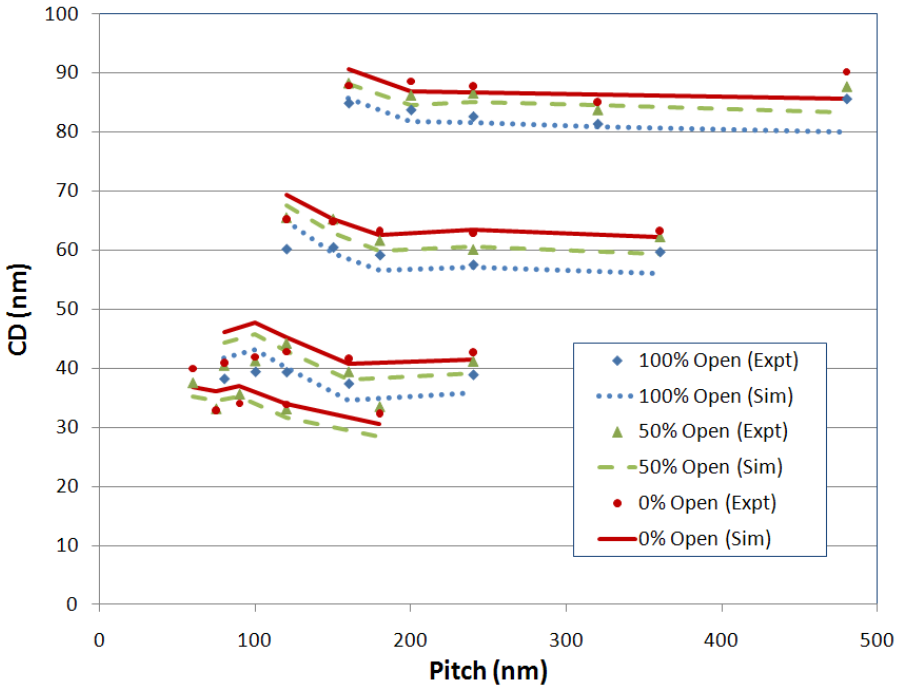

Figure 2: CD versus pitch curves within the flare test structures. Results are shown for 30nm, 40nm, 60nm, and 80nm lines. RMS error between simulation and experiment is 2.68nm.

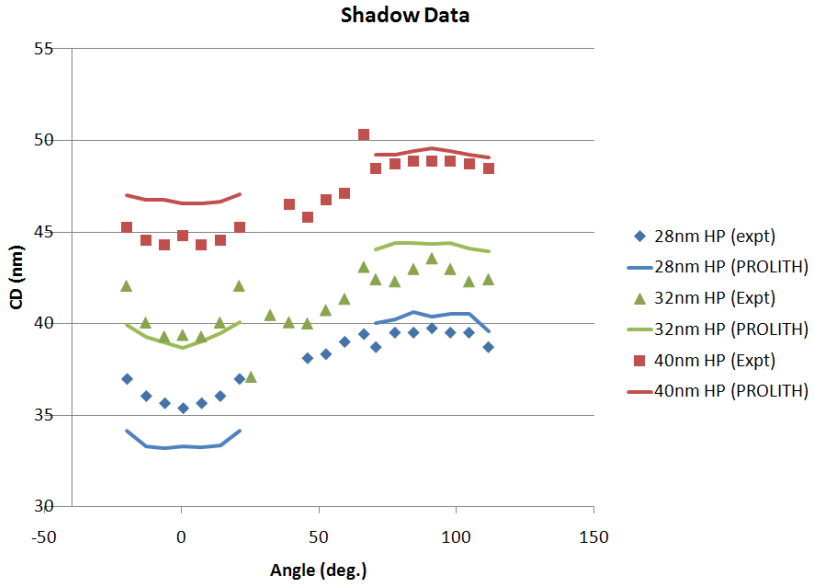

Figure 3: CD within the shadow test structure. RMS error between simulation and experiment is 1.64nm.

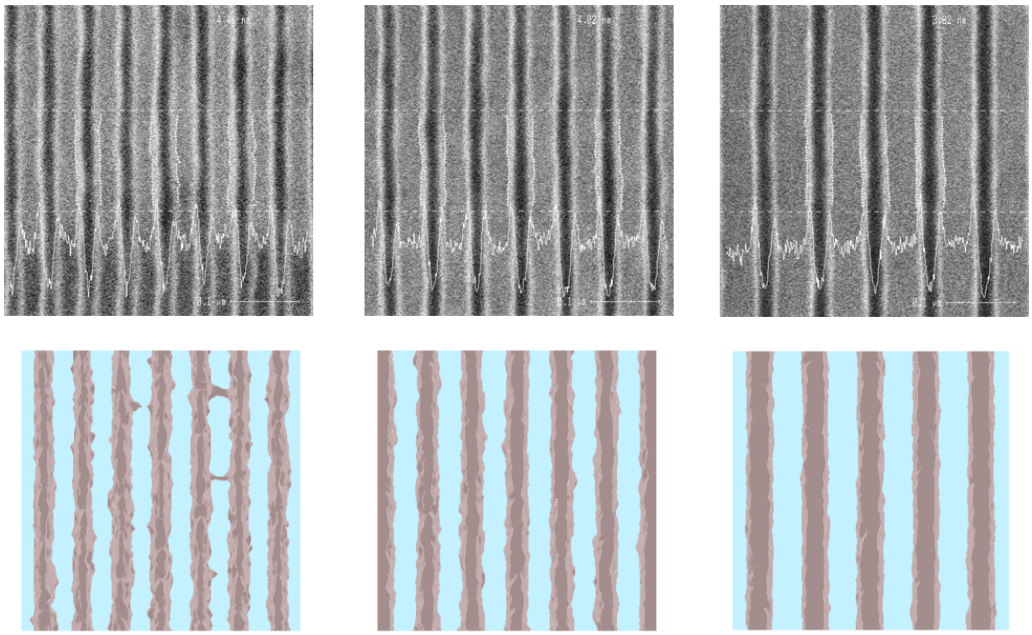

Figure 4: Experimental and simulated LWR. For the 28nm HP (shown left), experimental value is 4.46nm and simulated is 4.80nm. For 32nm HP (center), experimental value is 4.02nm and simulated is 3.98nm. For 40nm HP (right), experimental value is 3.82 and simulated is 3.26nm.

Influence of EUV exposure kinetics and resist formulation

The PROLITH Stochastic Resist has a special model for EUV exposure that describes the accepted mechanism for the exposure process at the 13.5nm wavelength [12]. Details of our model have been published elsewhere [13,14], but we briefly summarize here. The exposure process consists of three steps. First, a discrete photon is absorbed following shot noise (Poisson) statistics. Second, a photoelectron can be generated with a probability ϕ_e. The electron then propagates through the resist matrix, undergoing elastic and inelastic scattering events. During the inelastic scattering events, a secondary electron may be generated, which creates a cascade of electrons generated by the initial absorption of the photon. Finally, if one of these electrons moves within the reaction radius of a PAG molecule (R_{PAG}), then there is a probability that the PAG will be converted to an acid. The result of the exposure model calculation is a distribution of discrete acid molecule locations throughout the resist.

There are two important consequences of the EUV exposure mechanism compared with a mechanism where the PAG directly absorbs the photon. First, the acid is generated some finite distance away from the original photon absorption site, a phenomenon commonly called "photoelectron blur." Second, the acid yield, defined as the number of acids generated for each absorbed photon, can be larger than one. Both of these effects can be visualized by calculation of the acid point spread function, as shown in Figure 5. Here we show three acid PSFs corresponding to different values of the PAG reaction radius. Increasing the PAG reaction radius increases both the photoelectron blur and the acid yield – larger capture radii allows a larger number of PAG molecules to interact with a photoelectron, and it becomes more likely that an acid will be generated. In general, it is thought that increasing yield is beneficial because it should improve photospeed, but increasing blur will degrade image contrast. We are able to quantify these two effects in our model. Shown in Figure 6 is the dependence of dose-to-size and LWR on the overall yield. (The yield was manipulated by changing the reaction radius.) Increasing yield decreases the dose-to-size, but it also increases LWR

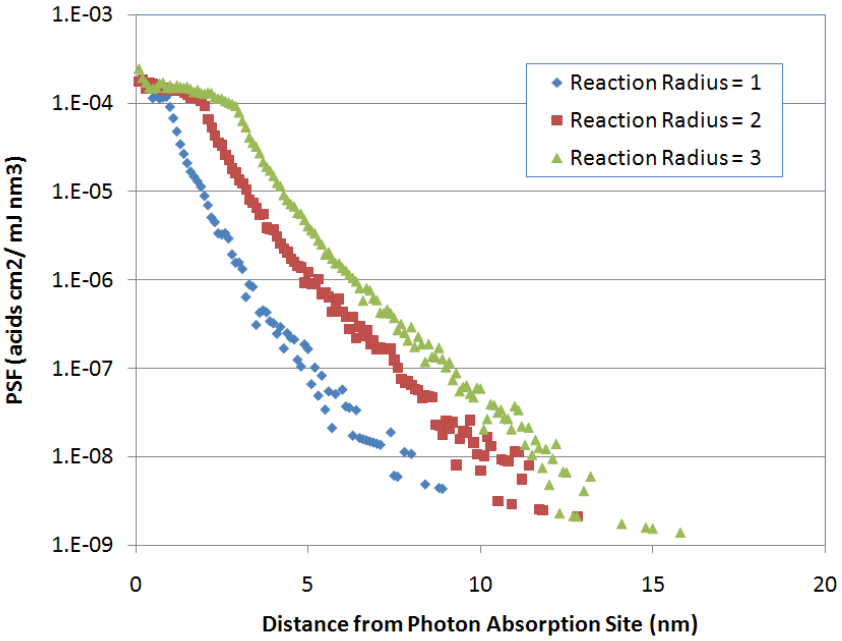

Figure 5: Acid generation point spread function during exposure for three different choices of the PAG reaction radius. For a reaction radius of 1nm, the overall yield (number of acids generated per absorbed photon) is 0.37. For radius of 2nm, the yield is 2.02, and for a radius of 3nm, the yield is 5.08. For all three PSF, 95% of the acids generated correspond to probabilities greater than 10^{-6}, so the size of the blur is around 2 to 4 nm.

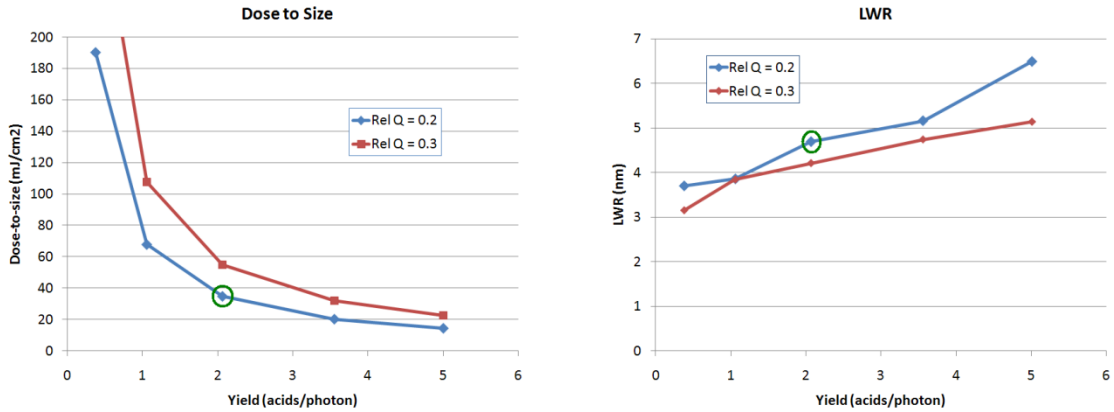

Figure 6: Effect of acid yield on dose-to-size (shown left), and LWR (shown right). Results are shown for relative quencher loadings of 0.2 and 0.3. The nominal parameters correspond to a yield of around 2 and a relative quencher loading of 0.2, and are designated by the circled point in each plot. Results were calculated for 30nm HP dense lines within 50% pattern density flare structure. The yield was changed by increasing the PAG-electron reaction radius (R_{PAG}) as shown in Figure 5.

One explanation for the increase in LWR with yield is that while the number of acids per absorbed photon is increased, the locations of these acids are highly correlated around the location where the initial photon was absorbed. If the acid molecules are often clumped into a small region, instead of spread throughout the resist, LWR increases.

It is well-known that the quencher loading modifies contrast and photospeed, so we decided to study the interaction between yield and quencher loading. The results in Figure 6 are shown for relative quencher loadings of 0.2 and 0.3, and as the relative quencher loading is increased photospeed is reduced and LWR is improved. Therefore, we might be able to simultaneously increase quencher loading and yield as a strategy to maintain a reasonable LWR and still improve the photospeed. This is shown by the quencher loading of 0.3 with a yield of 5 – the dose to size decreases from 38 mJ/cm2 to 22 mJ/cm2, while the LWR increases slightly from 4.8nm to around 5nm. Other combinations of quencher loading and yield might give additional improvements in sensitivity and LWR.

Influence of Aberrations and Flare Levels

Next, we would like to investigate the impact of optical upgrades and improvements, such as a reduction in flare and lens aberrations. We will assess these improvements by analyzing process windows in ProDATA™ from KLA-Tencor Corporation. First we will calculate process windows with flare and aberration levels typical of the ADT (the flare parameters and calibrated lens aberrations from the second section in this paper). Shown in Figure 7 are results for a focus-exposure matrix and the corresponding CD process window for the 30nm HP flare test structure with 0% open area. These results demonstrate a healthy 340nm DOF for a 5% exposure latitude specification. We also examined the LWR process window, as shown in Figure 8. Here we have set the LWR specification limit at 5nm, which is a very high tolerance. Despite this, the depth of focus is more constrained by LWR than CD, and the DOF is reduced to around 160nm. We can also examine other regions in the flare test structure, such as the 100% open structure. Here we find that the increased flare level degrades LWR, and the process window completely collapses. Overlapping CD and LWR process windows are shown in Figure 9 for the 0% open and for the 100% open area flare test structures.

We now can predict expected improvements for the EUV beta tools, with reduced aberrations (51 mλ instead of 91mλ) and half the flare. The lower aberrations and flare correspond to the levels reported for the ASML NXE3100 [16]. Here we see that both the exposure latitude (limited by CD excursions) and the depth of focus (limited by LWR) are improved. For 0% open area test structure, the depth of focus for 5% exposure latitude improves from 157nm to 198nm, and for the 100% open area test structure, the scanner with higher aberrations and flare has no DOF, while the improved scanner has 197nm DOF. It is clear that the improved optics will lead to much better LWR response, and improved process windows.

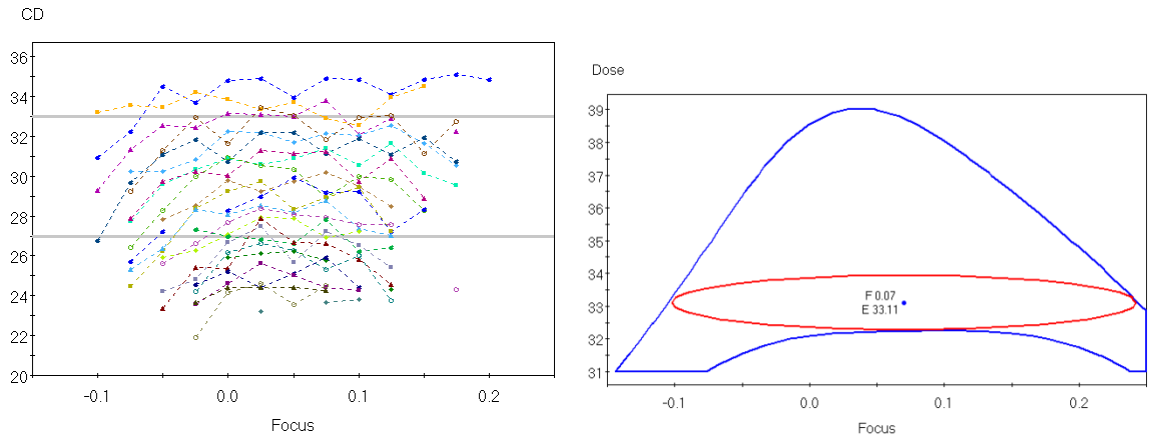

Figure 7: Simulated CD focus exposure matrix for 30nm HP lines within the flare test structure with 0% open area(left), and the corresponding CD process window (shown right). The CD process window has over 340nm depth of focus for a 5% exposure latitude specification.

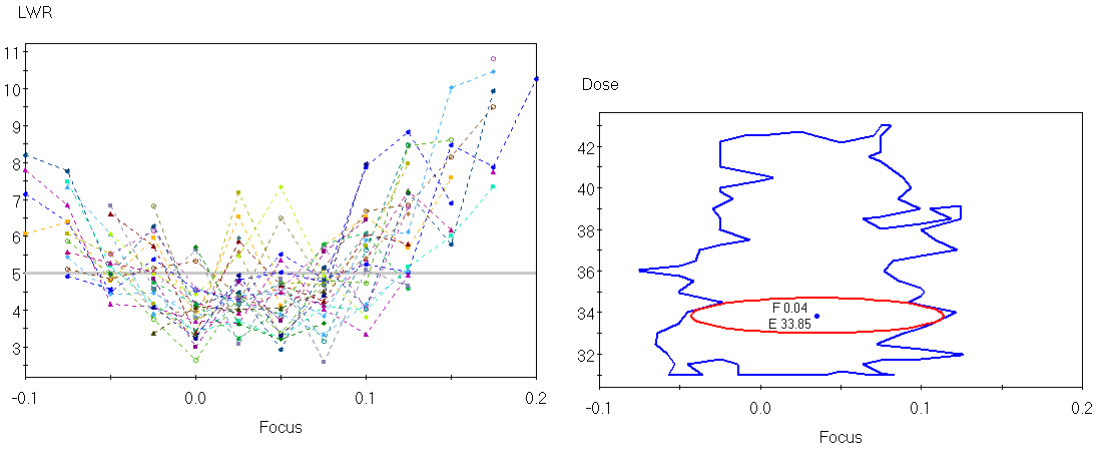

Figure 8: Simulated LWR focus exposure matrix for the same features shown in Figure 7. If we require a 5nm LWR specification, then LWR process window is shown on the right. For a 5% exposure latitude specification, there is 156nm DOF.

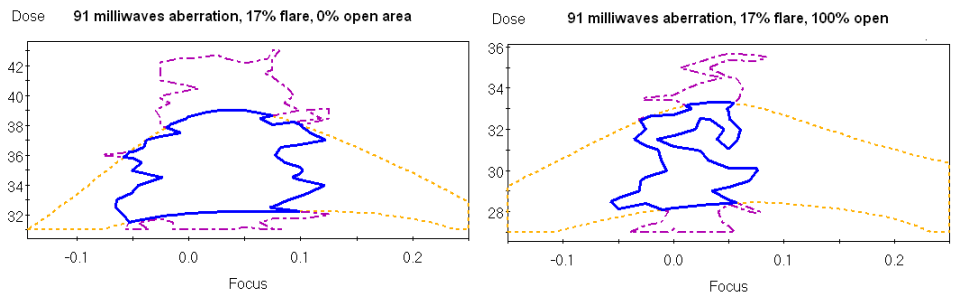

Figure 9: Process windows for 30nm HP structures within the flare test structure for 0% open area (left) and 100% open area (right). The flare and aberration levels correspond to the values calibrated from the ADT dataset. CD process windows are shown in dashed yellow, LWR process windows with a 5nm specification are shown in purple dash-dot, and the overlap is shown with a solid blue line.

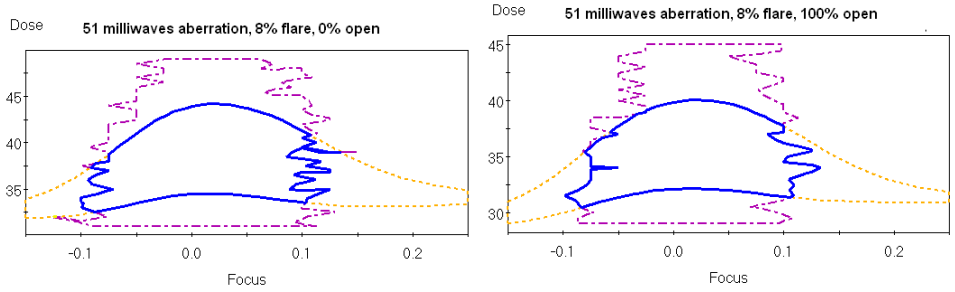

Figure 10: Process windows for 30nm HP structures within the flare test structure for 0% open area (left) and 100% open area (right). The flare and aberration levels are reduced to levels typical of the beta EUV tools. CD process windows are shown in dashed yellow, LWR process windows with a 5nm specification are shown in purple dash-dot, and the overlap is shown with a solid blue line.

Summary and Conclusions

We have presented a comprehensive EUV lithography model that includes both the most important optical effects (mask shadowing and flare) and the most important resist effects (exposure yield, photoelectron blur, and LWR). The parameters in both the optical and resist models were calibrated to a set of data from the ASML ADT at IMEC. We then used the model to investigate the size of the photoelectron blur, and the impact of acid yield on photospeed and LWR. As expected, increasing yield gave better photospeed, but it also degraded the LWR response. We then investigated the interaction between exposure yield and quencher loading, and we found that there were combinations where photospeed could be improved with only a small increase in LWR.

Improvements to lens aberration levels and flare were evaluated by simulation of CD and LWR process windows. For aberrations and flare typical of the ASML ADT, we found that the LWR process window completely collapsed with for 30nm HP features when the surrounding area was 100% open. For the improved aberration and flare levels expected for the beta tools, the process windows were improved to around 200nm DOF for a 5% exposure latitude specification. For all cases simulated in this study, the process windows were constrained by the LWR specification. This means that process windows based on CD specification alone are not an accurate reflection of what is required for a robust, manufacturable process, and that a comprehensive lithography model is required in order to evaluate the lithography as a system, not a set of independent components.

References

1. J.W. Goodman, *Statistical Optics*, John Wiley & Sons, New York (1985).

2. D.G. Sterns, D.P. Gaines, and D.W. Sweeney, "Nonspecular x-ray scattering in a multilayer-coated imaging system," *Applied Optics,* Vol. 84 (1998) 1003.

3. K. Lai, C. Wu, and C. Progler, "Scattered light: the increasing problem for 193nm exposure tools and beyond," *Proceedings of SPIE,* Vol. 4346 (2001) 1424.

4. C. Krautschik, M. Ito, I. Nishiyama, and S. Okazaki, "Impact of EUV light scatter on CD control as a result of mask density changes," *Proceedings of SPIE*, Vol. 4688 (2002) 289.

5. Y.C. Kim, P. De Bisschop, and G. Vandenberghe, "Evaluation of stray light and quantitative analysis of its impact on lithography," *Journal of Microlithography, Microfabrication, and Microsystems,* Vol. 4 (2005) 043002.

6. G.F. Lorusso, A.M. Goethals, R. Jonckheere, J. Hermans, K. Ronse, A.N. Myers, I. Kim, A. Niroomand, F. Iwamoto, and D. Ritter, "Extreme ultraviolet lithography at IMEC: Shadowing Compensation and flare mitigation strategy," *Journal of Vacuum Science and Technology B,* Vol. 25 (2007) 2127.

7. G. F. Lorusso, F. Van Roey, E. Hendrickx, G. Fenger, M. Lam, C. Zuniga, M. Habib, H. Diab, and J. Word, "Flare in extreme ultraviolet lithography: metrology, out-of-band radiation, fractal point-spread function, and flare map calibration," *Journal of Micro/Nanolithography, MEMS, and MOEMS,* Vol. 8 (2009) 041505.

8. J. Lee, K. Song, C. Kim, Y. Kim, and O. Kim, "A study of flare variation in extreme ultraviolet lithography for sub-22nm line and space pattern," *Japanese Journal of Applied Physics,* Vol. 49, (2010) 06GD09.

9. AreaFill v1.54 is from Artwork Conversion Software, Inc. (http://www.artwork.com)

10. Y. Arisawa, H. Aoyama, T. Uno, and T. Tanaka, "EUV flare correction for the half-pitch 22-nm node," *Proceedings of SPIE,* Vol. 7636 (2010) 763618.

11. K. Adam, and A. Neureuther, "Domain decomposition methods for the rapid electromagnetic simulation of photomask scattering," *Journal of Micro/Nanolithography, MEMS, and MOEMS,* Vol. 1 (2002) 253.

12. T. Kozawa, and S. Tagawa, "Radiation chemistry in chemically amplified resists," *Japanese Journal of Applied Physics,* Vol. 49 (2010) 030001.

13. J.J. Biafore, M.D. Smith, C.A. Mack, J.W. Thackeray, R. Gronheid, S.A. Robertson, T. Graves, and D. Blankenship, "Statistical simulation of photoresists at EUV and ArF," *Proceedings of SPIE,* Vol. 7273 (2009) 727343.

14. J.J. Biafore, M.D. Smith, E. van Setten, T. Wallow, P. Naulleau, D. Blankenship S.A. Robertson, and Y. Deng, "Resist pattern prediction at EUV," *Proceedings of SPIE,* Vol. 7636 (2010) 76360R.

15. S.A. Robertson, J.J. Biafore, M.D. Smith, M.T. Reilly, and J. Wandell, "Stochastic simulation of resist linewidth roughness and critical dimension uniformity for optical lithography," *Journal of Micro/Nanolithography, MEMS, and MOEMS,* Vol. 9 (2010) 041212.

16. M. Lowisch, P. Kuerz, H.J. Mann, O. Natt, and B. Thuering, "Optics for EUV production," *Proceedings of SPIE*, Vol. 7636 (2010) 763603.